Monthly Notices
of the
ROYAL ASTRONOMICAL SOCIETY

MNRAS **447,** 3548–3563 (2015) doi:10.1093/mnras/stu2713

The star formation main sequence and stellar mass assembly of galaxies in the Illustris simulation

Martin Sparre,[1⋆] Christopher C. Hayward,[2,3†] Volker Springel,[3,4] Mark Vogelsberger,[5] Shy Genel,[6] Paul Torrey,[2,5,6] Dylan Nelson,[6] Debora Sijacki[7] and Lars Hernquist[6]

[1]*Dark Cosmology Centre, Niels Bohr Institute, University of Copenhagen, Juliane Maries Vej 30, DK-2100 Copenhagen, Denmark*
[2]*TAPIR, Mailcode 350-17, California Institute of Technology, Pasadena, CA 91125, USA*
[3]*Heidelberger Institut für Theoretische Studien, Schloss-Wolfsbrunnenweg 35, D-69118 Heidelberg, Germany*
[4]*Zentrum für Astronomie der Universität Heidelberg, Astronomisches Recheninstitut, Mönchhofstrasse 12-14, D-69120 Heidelberg, Germany*
[5]*Department of Physics, Kavli Institute for Astrophysics and Space Research, Massachusetts Institute of Technology, Cambridge, MA 02139, USA*
[6]*Harvard–Smithsonian Center for Astrophysics, 60 Garden Street, Cambridge, MA 02138, USA*
[7]*Kavli Institute for Cosmology, Cambridge, and Institute of Astronomy, Madingley Road, Cambridge CB3 0HA, UK*

Accepted 2014 December 18. Received 2014 December 18; in original form 2014 August 28

ABSTRACT

Understanding the physical processes that drive star formation is a key challenge for galaxy formation models. In this paper, we study the tight correlation between the star formation rate (SFR) and stellar mass of galaxies at a given redshift, how halo growth influences star formation, and star formation histories of individual galaxies. We study these topics using Illustris, a state-of-the-art cosmological hydrodynamical simulation of galaxy formation. Illustris reproduces the observed relation (the star formation main sequence, SFMS) between SFR and stellar mass at redshifts $z = 0$ and 4, but at intermediate redshifts of $z \simeq 1$–2, the simulated SFMS has a significantly lower normalization than reported by observations. The scatter in the relation is consistent with the observed scatter. However, the fraction of outliers above the SFR–stellar mass relation in Illustris is less than that observed. Galaxies with halo masses of $\sim 10^{12}\,\mathrm{M}_{\odot}$ dominate the SFR density of the Universe, in agreement with the results of abundance matching. Furthermore, more-massive galaxies tend to form the bulk of their stars at high redshift, which indicates that 'downsizing' occurs in Illustris. We also studied the star formation histories of individual galaxies, including the use of a principal component analysis decomposition. We find that for fixed stellar mass, galaxies that form earlier have more-massive black holes at $z = 0$, indicating that star formation and black hole growth are tightly linked processes in Illustris. While many of the properties of normal star-forming galaxies are well reproduced in the Illustris simulation, forming a realistic population of starbursts will likely require higher resolution and probably a more sophisticated treatment of star formation and feedback from stars and black holes.

Key words: methods: numerical – galaxies: evolution – galaxies: formation – galaxies: starburst – galaxies: star formation – cosmology: theory.

1 INTRODUCTION

In the Λ cold dark matter (ΛCDM) paradigm, galaxies reside in dark matter haloes that are built up hierarchically as gravity amplifies perturbations created in the early Universe (Zel'dovich 1970). The structure and sub-structure of dark matter haloes, and the cosmic web surrounding them, have been intensively studied using numerical simulations (e.g. Springel et al. 2005b; Diemand et al. 2008; Klypin, Trujillo-Gomez & Primack 2011), in which the dark matter is modelled as collisionless particles that interact with each other only through gravity. In the last decade, such simulations have led to a general consensus about the distribution of dark matter on large scales. However, the formation and evolution of the baryons embedded in these haloes are far from understood. In the canonical theory of galaxy formation (e.g. Rees & Ostriker 1977; Silk 1977; White & Rees 1978), galaxies form stars when hot gas radiates away energy, cools and loses pressure support. The evolution of such galaxies is further influenced by their merger history, accretion

⋆E-mail: sparre@dark-cosmology.dk
†Moore Prize Postdoctoral Scholar in Theoretical Astrophysics.

of gas and dark matter, and regulation of star formation by feedback processes related to stellar winds, supernovae and active galactic nuclei (AGN). Much of our understanding of galaxies is based on observed relations and physical modelling of galaxy structure. Important observations include the relation between luminosity and velocity widths of galaxies (Faber & Jackson 1976; Tully & Fisher 1977), the global star formation rate (SFR) as a function of redshift (Lilly et al. 1996; Madau, Pozzetti & Dickinson 1998), relations between mass and metallicity (Tremonti et al. 2004; Mannucci et al. 2010), global star formation laws (Schmidt 1959; Kennicutt 1998) and the morphologies of galaxies (Hubble 1926; Dressler 1980).

A recently established relation is the so-called star formation main sequence (SFMS), which is an approximately linear relation between the SFR and the stellar mass ($M_\star$) of star-forming galaxies. The relation exists at both low ($z < 1$; Brinchmann et al. 2004; Salim et al. 2007) and high ($z \gtrsim 1$; Daddi et al. 2007) redshift and is recovered in optical (Tasca et al. 2014), infrared (Elbaz et al. 2011) and radio observations (Karim et al. 2011). It is a tight relation in the sense that the scatter around the relation is small (e.g. Speagle et al. 2014 reports a scatter of $\sigma \simeq 0.2$ dex). The normalization of the SFMS is observed to increase from $z = 0$ to 2, the redshift at which the global SFR density (SFRD) peaks. The tightness of the SFMS and the fact that most star-forming galaxies lie on it imply that the bulk of the star formation in the Universe occurs in a quasi-steady state (Noeske et al. 2007) and that the fraction of a given star-forming galaxy's lifetime during which it lies significantly above the SFMS because of e.g. merger-induced starbursts is small.[1]. Thus, it is important to not equate galaxies that lie above the SFMS with mergers. Instead, galaxies above the SFMS should be referred to as 'starbursts' (by definition), which may or may not be merger induced. Galaxies on the SFMS should be considered 'quiescently star forming', and such galaxies may still be involved in an ongoing merger.

In addition to characterizing star-forming galaxies, the SFMS also provides a natural way to define starbursts as galaxies with SFRs well above the SFMS value for their stellar mass and redshift (Rodighiero et al. 2011; Sargent et al. 2012; Atek et al. 2014). Despite having large SFRs compared with normal galaxies, starbursts account for only a small fraction (∼5–10 per cent) of the global SFRD (Rodighiero et al. 2011) because they are rare and short lived (because of their short gas-consumption time-scales; Knapen & James 2009; Daddi et al. 2010; Genzel et al. 2010). This minor contribution of starbursts to the total SFRD is consistent with semi-empirical models for infrared galaxy number counts (Béthermin et al. 2012) and luminosity functions (Hopkins et al. 2010). 'Red and dead' or quiescent galaxies are galaxies that lie significantly below the SFMS. These galaxies are typically elliptical galaxies (Wuyts et al. 2011) with little gas available for star formation. They are likely the descendants of starbursts after their intense star formation has been quenched by feedback from AGN (Sanders et al. 1988; Cemile Marsan et al. 2014; Toft et al. 2014) or other processes. Because we are interested in actively star-forming galaxies, we will largely ignore the quiescent galaxy population in this work.

[1] It is sometimes claimed that galaxies on the SFMS must not be undergoing mergers. This is a misconception: for most of the duration of mergers, the SFR is not elevated significantly by the interaction (e.g. Cox et al. 2008; Hopkins et al. 2010). Consequently, merging galaxies often lie on the SFMS (see fig. 1 1 of Hayward et al. 2012; Puech et al. 2014 also finds major mergers to be on the SFMS during most of the merger process

Several attempts have been made to reproduce the SFMS in hydrodynamical simulations of galaxies (Davé, Oppenheimer & Finlator 2011; Kannan et al. 2014; Torrey et al. 2014a) and (semi-) analytical models (Dutton, van den Bosch & Dekel 2010; Davé, Finlator & Oppenheimer 2012; Dekel et al. 2013). With both methods, a tight relationship between SFR and stellar mass can be recovered. However, reproducing the evolution of the normalization is a challenge for theoretical models (Davé 2008; Damen et al. 2009). The main problem is producing the correct normalization at both $z = 0$ and 2. Potential solutions to this problem have been suggested, including a varying initial mass function (IMF; Davé 2008) and modification of the time-scale for reincorporation of gas ejected by feedback processes (Mitchell et al. 2014).

A different important characteristic of a population of galaxies is the connection between the growth of haloes and the formation of stars inside them. Dark matter haloes build up hierarchically through accretion and mergers. The formation of stars is a more complex phenomenon that is heavily influenced by feedback processes and gas cooling. By matching the abundance of haloes in cosmological dark matter simulations to real observations of galaxies, it has been shown that stars form most efficiently in $\simeq 10^{12}\,\mathrm{M}_\odot$ haloes (Behroozi, Wechsler & Conroy 2013a, b; Moster, Naab & White 2013; Kravtsov, Vikhlinin & Meshscheryakov 2014), which is believed to occur because star formation is suppressed by stellar feedback and feedback from AGN at lower and higher halo masses, respectively (Vogelsberger et al. 2013; Torrey et al. 2014a; Schaye et al. 2015). An implication is that galaxies that reside in massive (e.g. $\sim 10^{14}\,\mathrm{M}_\odot$ at $z = 0$) haloes formed their stars earlier than galaxies that reside in $\sim 10^{12}\,\mathrm{M}_\odot$ haloes (at $z = 0$) because galaxies inside $10^{12}\,\mathrm{M}_\odot$ haloes at $z = 0$ are still forming stars with the highest possible efficiency. A consequence of this complicated relation between halo growth and star formation is the 'downsizing' scenario, in which the galaxies with the most-massive stellar components (e.g. $M_\star \sim 10^{11}\,\mathrm{M}_\odot$) at $z = 0$ formed their stars earlier than galaxies of more-moderate masses (e.g. $M_\star \sim 10^{10}\,\mathrm{M}_\odot$).

The aim of this paper is to study properties of star-forming galaxies, especially the SFMS and the relation between halo growth and star formation, in the Illustris cosmological simulation. Section 2 describes Illustris, Section 3 analyses properties of the SFMS and Section 4 examines how the halo mass affects star formation in galaxies. In Section 5, we study star formation histories (SFHs) of galaxies, and we examine how the SFH of a galaxy depends on its dark matter halo mass and black hole mass. In Section 6, we use the results from the previous sections to study the origin of the scatter in the SFMS. We discuss our findings in Section 7 and summarize our conclusions in Section 8.

2 THE ILLUSTRIS SIMULATION

Illustris is a cosmological hydrodynamical simulation of a comoving volume of $(106.5\,\mathrm{Mpc})^3$. The cosmological model used in Illustris is the ΛCDM cosmology with parameters from the *WMAP*7 data release (Hinshaw et al. 2013). Besides gravity and hydrodynamics, it includes treatments of gas cooling, star formation and feedback from stellar winds, supernovae and AGN (see Vogelsberger et al. 2013, 2014a,b; Torrey et al. 2014a). The Illustris simulation has previously been used to study a range of different galaxy properties, such as the evolution of damped Lyα absorbers (Bird et al. 2014), the formation of elliptical and spiral galaxies (Vogelsberger et al. 2014b), the evolution of galaxy properties from high to low redshift (Genel et al. 2014) and the relation between the dark matter and

stellar components in the faint outskirts of galaxies (Pillepich et al. 2014).

The initial conditions at a redshift of $z = 127$ include 1820^3 dark matter particles, 1820^3 gas cells and 1820^3 Monte Carlo tracer particles (Genel et al. 2013). The gravitational softening length for the dark matter particles is 1420 comoving pc. The gravitational softening lengths of the gas cells depend on the cell size; they have a minimum value of 710 physical pc. Star particles have a softening length of 1420 comoving pc at $z \geq 1$, and at lower redshifts, the softening length is fixed to 710 physical pc. The mass of the dark matter particles is $6.26 \times 10^6\,\mathrm{M}_\odot$, and the gas cell target mass is $1.26 \times 10^6\,\mathrm{M}_\odot$. In this paper, we will also study a simulation with lower resolution (a total of 3×910^3 dark matter, gas and tracer particles, implying eight times worse mass resolution and two times poorer spatial resolution), but with the same physical galaxy formation model. We will refer to this simulation as the *Illustris low-resolution run*.

The hydrodynamical calculations in Illustris are done with the AREPO code (Springel 2010), where the hydrodynamical forces are computed on a moving mesh built with a Voronoi tessellation. With a spatial resolution of $\simeq 1$ kpc, there is no hope to resolve giant molecular clouds, where star formation takes place in the Universe. Instead a sub-resolution model is implemented (Springel & Hernquist 2003; Vogelsberger et al. 2013, 2014a), where unresolved physical processes such as the formation of molecular clouds, thermal instabilities and supernova feedback are coarsely described with an effective equation of state. When a gas cell exceeds a hydrogen number density of $\rho_{\rm th} = 0.13\,\mathrm{cm}^{-3}$, it produces star particles stochastically on a density-dependent time-scale of

$$t_*(\rho) = t_0^* \left(\frac{\rho}{\rho_{\rm th}}\right)^{-1/2}, \quad (1)$$

where $t_0^* = 2.2$ Gyr. With the chosen values of $\rho_{\rm th}$ and t_0^*, galaxies obey the empirical Kennicutt–Schmidt relation between the gas surface density and the SFR per surface area of a galaxy (Kennicutt 1989). A star particle in this model represents an entire stellar population born with a Chabrier IMF (Chabrier 2003). During each timestep of the simulation, the amount of H, He, C, N, O, Ne, Mg, Si and Fe released by each stellar population is calculated and returned to the gas.

The formation of stars is accompanied by the release of kinetic winds from supernovae, which contribute to expelling the surrounding gas and to the chemical enrichment of the interstellar gas. The wind velocity is 3.7 times the one-dimensional velocity dispersion of the dark matter near the star-forming region.

In friends-of-friends groups, more massive than $1.7 \times 10^{10}\,\mathrm{M}_\odot$ black holes are seeded, and a model of AGN feedback is included (Springel, Di Matteo & Hernquist 2005a; Sijacki et al. 2007), where a quasar can be in a radio-quiet or radio-loud mode. In the latter mode, thermal energy is injected into the gas surrounding the black hole. Also included is a treatment of AGN radiative feedback, which heats the gas surrounding the AGN and changes its ionization state (see full description in Vogelsberger et al. 2013).

Also implemented are processes such as radiative cooling, chemical evolution and an ultraviolet background. For a full description of the physical model of Illustris, see Vogelsberger et al. (2013) and Torrey et al. (2014a).

3 THE STAR FORMATION MAIN SEQUENCE

An SFMS that relates the SFR and the stellar mass of galaxies is recovered in Illustris; see Fig. 1, which shows the relation at $z = 0$, 1, 2 and 4. The SFMS is plotted in terms of both the SFR and specific SFR, SSFR $\equiv$ SFR$/M_\star$, versus $M_\star$. The simulation is compared with the compilation of observations by Behroozi et al. (2013b, table 8), who fit a relation to a large number of measurements from different authors and quantified the scatter in the observations of the SFMS from different publications. This scatter, which is denoted by the error bars in Fig. 1, quantifies the interpublication variance of the SFMS and therefore accounts for the systematic error arising when measuring the SFMS with different methods. The normalization in Illustris agrees with the observational constraints from Behroozi et al. (2013b) at $z = 0$. The figure also shows that the normalization of the SFMS in Illustris is well converged above $M_\star = 10^9\,\mathrm{M}_\odot$.

At $z = 4$, Illustris is also in good agreement with the observed relation. However, despite being in good agreement at $z = 0$ and 4, the normalization of the SFMS is significantly lower than the observational constraints at intermediate redshifts of $z = 1$ and 2 (this has been previously noted and discussed for Illustris; see Genel et al. 2014). Several studies have previously pointed out discrepancies between the observed SFMS relation and galaxy formation models (e.g. Daddi et al. 2007; Davé 2008; Damen et al. 2009), especially at $z \simeq 2$.

The SSFR in Illustris becomes approximately independent of mass for $M_\star < 10^{10.5}\,\mathrm{M}_\odot$ (Fig. 1, *lower panels*), which is a small but remarkable difference from the observations of Behroozi et al. (2013b), which indicate a declining SSFR as function of mass. Fig. 2 shows the redshift evolution of the SSFR for galaxies with different stellar masses. The SSFR is here determined by calculating the normalization of the SFMS in different stellar mass bins. Since the SSFR is independent of mass at fixed redshift in Illustris, the SSFRs of galaxies from different mass bins have the same redshift evolution. The fitting relations from Behroozi et al. (2013b) show a somewhat different evolution, partially because the SSFR is mass dependent at fixed redshift. We note that the problem with reproducing the evolution of the SSFR (in Fig. 2) is closely related to the problem of reproducing the normalization of the SFMS at $z = 1$ and 2 (in Fig. 1). The different behaviour of SSFR(z) in Illustris and observations also shows that the good match of the SFMS to observations at $z \simeq 4$ is most likely a coincidence.

The tensions between the observed and simulated SSFR are consistent with the lack of a sharp cut-off of the stellar mass function in Illustris (Genel et al. 2014; Vogelsberger et al. 2014a) and the star formation efficiency peak in Illustris (Vogelsberger et al. 2014a) being broader than that derived with abundance matching by Behroozi et al. (2013b). Genel et al. (2014) also studied the redshift evolution of the SSFR in Illustris and found that the SSFR of galaxies is closely tied to the galaxies' dark matter accretion rate. In our model, the velocities of the stellar winds scale in proportion to the local dark matter velocity dispersion. Therefore, a natural explanation for the tensions outlined above is that the star formation and feedback processes are too closely linked to the dark matter evolution in Illustris.

In Fig. 2, we also compare our results with the analytical model from Mitra et al. (2014). This model relies on an analytical approximation of halo growth from a cosmological simulation (Dekel et al. 2009a). The SFR of a galaxy associated with a halo is determined from the equilibrium assumption that the gas mass in the

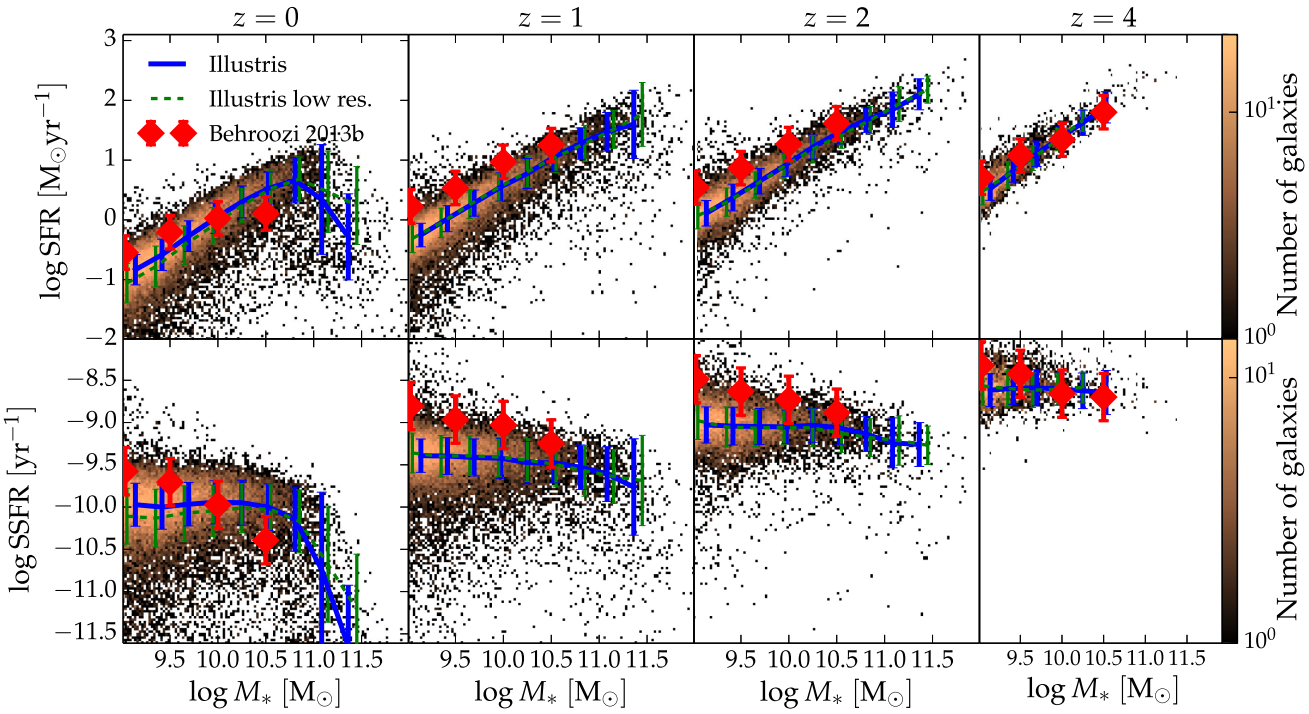

Figure 1. The SFMS at $z = 0$, 1, 2 and 4 for the Illustris simulation (the two-dimensional histogram in the background). The upper panels show the median SFR, and the lower panels show the median SSFR. The simulation results are compared to the compilation of observations from Behroozi et al. (2013b), where the error bars indicate 68 per cent confidence intervals for the interpublication variance. The solid and dashed lines indicate the median relation from the low-resolution and high-resolution versions of Illustris, respectively, and the associated error bars denote the 1σ errors estimated by fitting Gaussian functions to the SFR distributions of galaxies in narrow mass bins.

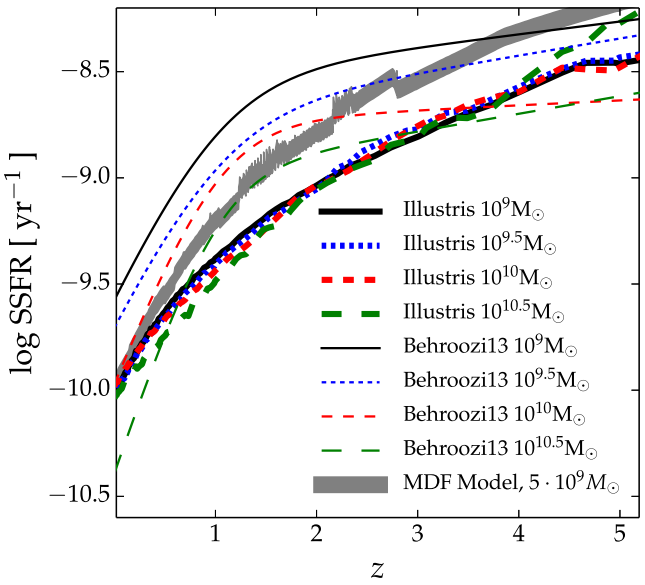

Figure 2. The median SSFR as function of redshift for galaxies with different stellar masses. At each redshift, the SSFR of galaxies in the given stellar mass bin is computed. The thin lines show the compilation of observations from Behroozi et al. (2013b), and the thick lines show the evolution in Illustris. The grey shaded regions show the analytical model from Mitra, Davé & Finlator (2014). The different evolution of the SSFR from $z = 4$ to 0 is closely related to the too low normalization of the SFMS at $z = 1$ and 2 in Fig. 1.

interstellar medium (ISM) is non-evolving. The baryon accretion rate, mass loading of stellar winds, feedback processes that prevent gas from entering a galaxy and the time-scale for reincorporating gas ejected by feedback are all closely tied to the dark matter growth rate. The eight free parameters used to control these feedback processes have been fit with a Monte Carlo Markov Chain method to maximize the agreement with the SFMS, mass–metallicity relation and halo-mass–stellar mass relation at $z = 0$, 1 and 2. This model is one of many similar analytical galaxy formation models (Bouché et al. 2010; Davé, Finlator & Oppenheimer 2012; Lilly et al. 2013; Dekel & Mandelker 2014). As in Illustris, the SSFR at $z < 2$ is underpredicted by the Mitra et al. (2014) model. This supports our conclusion that it is necessary to untie the feedback processes from the dark matter growth rate in order to reproduce the observed evolution of the SSFR of galaxies. Mitra et al. (2014) matches the observations slightly better than Illustris. This is likely because it is computationally cheaper to tune model parameters in an analytical model than in a cosmological simulation.

3.1 The scatter in the main sequence

The intrinsic scatter in the galaxy main sequence is predicted to be driven by the different gas accretion histories of different galaxies (see the analytical modelling of Dutton et al. 2010), and it has been suggested that the small scatter in the SFMS can be understood by applying the central limit theorem to star-forming galaxies (Kelson 2014). Observations typically reveal a scatter of 0.21–0.39 dex (this reflects the range of values given in table 9 in Behroozi et al. 2013b), but the measured scatter will of course depend on the exact selection criteria for the star-forming galaxies which form the main sequence

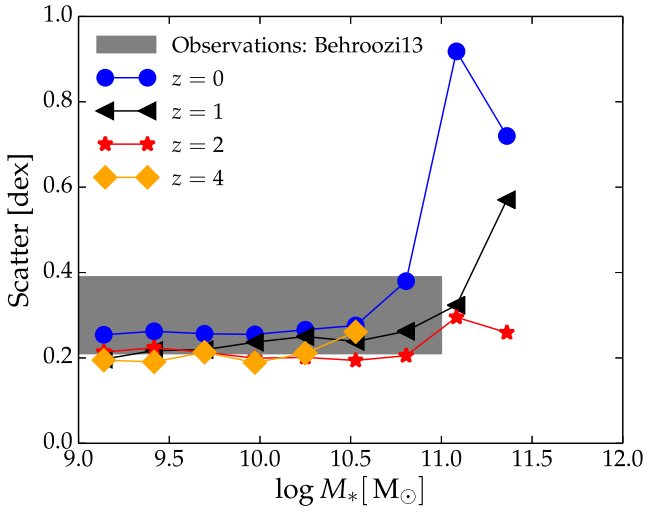

Figure 3. The scatter in the main sequence as function of mass for four different redshifts. The grey box shows the range of scatter in typical observations (from Behroozi et al. 2013b). Above 10^{11} M$_\odot$, there are no reliable observational constraints for the scatter.

(e.g. Whitaker et al. 2012) as well as on the uncertainties in SFR indicators.

To measure the scatter in the SFMS, we perform a Gaussian fit to the distributions of SFRs in different stellar mass bins. This method is similar to what is used in Rodighiero et al. (2011). In Fig. 3, we show the scatter in the Illustris galaxies' SFR values as function of stellar mass for four different redshifts. Below $10^{10.5}$ M$_\odot$, the scatter is constant at 0.2–0.3 dex at each redshift, which is in excellent agreement with observational constraints. At the high-mass end ($M_* > 10^{10.5}$ M$_\odot$), the scatter deviates from the value at lower masses because the galaxy main sequence is ill-defined at these high masses in Illustris (this is also seen in Fig. 1).

3.2 Star formation above the main-sequence relation

After having examined the behaviour of the main-sequence relation and its scatter in the Illustris simulation, we will now look at starburst galaxies that lie significantly above the main-sequence relation. In Fig. 4, the fraction of stars formed in galaxies on and above the main sequence is computed at different redshifts. We define a galaxy to be on the main-sequence relation if the SFR is within 2.5σ of the SFMS relation, which is the same criterion used in Rodighiero et al. (2011). For $M_* > 10^{10}$ M$_\odot$, the fraction of stellar mass formed in galaxies above the SFMS relation is lower than the observational result reported by Rodighiero et al. (2011) at $1.5 < z < 2.5$. We also note that the fraction of star formation that occurs above the main sequence is consistent in the high- and low-resolution Illustris runs for $M_* > 10^{9.5}$ M$_\odot$. In Section 7.2, we will further discuss the paucity of starbursts in Illustris.

3.3 The choice of SFR indicator

The SFR of a galaxy can be inferred using different diagnostics, such as the Hα luminosity, the ultraviolet luminosity or the total infrared luminosity (Kennicutt & Evans 2012). Different diagnostics are sensitive to the past SFR in a galaxy smoothed over different time-scales, so if a galaxy has a very rapidly changing SFR, different indicators will yield different SFR values. The time-scale for which different indicators are sensitive can vary from tens to hundreds of

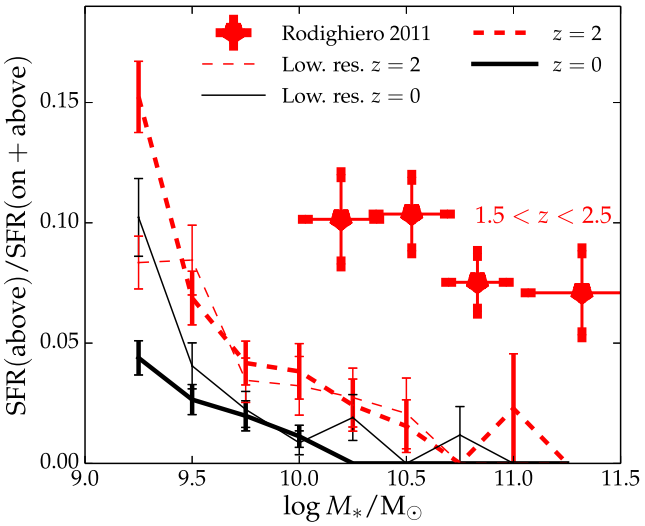

Figure 4. The fraction of stellar mass formed by galaxies 2.5σ or higher above the SFMS at $z = 0$ and 2 (solid and dashed, respectively). The thick and thin lines show the high- and low-resolution Illustris runs, respectively. The error bars indicate the contribution of Poisson noise. The simulated galaxy distribution is compared to the observational measurement at $1.5 < z < 2.5$ from Rodighiero et al. (2011).

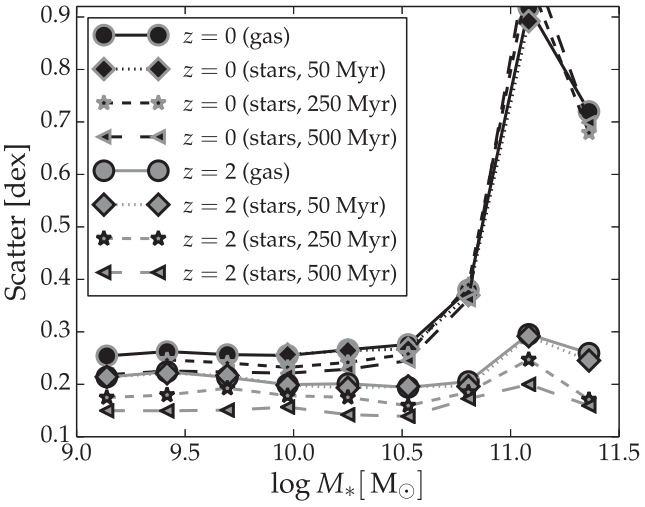

Figure 5. The main sequence scatter at $z = 0$ and 2 with the SFR measured in four different ways: from the instantaneous gas properties, and from the initial mass of the stars formed in the last 50, 250 and 500 Myr in the galaxies. When estimating the SFR from the stars formed in the last 500 Myr, the scatter is lower than in the other cases.

megayears. A situation in which one has to be particularly careful to rely on such averaging is in the post-starburst phase of merging galaxies, where simulations show that the SFR inferred from the total infrared luminosity overestimates the actual SFR of a galaxy by as much as two orders of magnitudes (Hayward et al. 2014b).

In Fig. 5, the scatter in the main sequence is shown for four different definitions of the SFR. First, the SFR is calculated from the instantaneous gas properties of galaxies, which we regard as the true SFR of the galaxies. We additionally calculate the mean SFR from the mass of stars formed in the last 50, 250 and 500 Myr in a galaxy. The scatter in the main sequence is essentially the same in the cases where the SFR is calculated from the gas or the stars formed during the last 50 Myr. For the case where the SFR is

calculated from the mass of stars formed in the last 250 Myr, the scatter in the main sequence decreases by 0.03 dex at both $z = 0$ and 2, and when averaged over 500 Myr, the scatter decreases by 0.05 dex. It is not surprising that the scatter declines when increasing the time over which the SFR is averaged, since the SFHs of galaxies are more similar when variability on a time-scale smaller than e.g. 500 Myr is smoothed out.

For actively star-forming galaxies, most of the widely used SFR indicators are sensitive to time-scales smaller than 200 Myr (Kennicutt & Evans 2012). Thus, we conclude that the time-scale over which the SFR indicator is sensitive is very unlikely to change the derived scatter in the main-sequence relation for the physics model used in Illustris, for which star formation is less bursty than in reality. The systematic offsets between different indicators are likely of much greater importance.

It is possible that the role of the characteristic time-scale of an SFR indicator will have an impact on the derived SFR for feedback models other than the one used in Illustris. Hopkins et al. (2014) and Governato et al. (2014), for example, present feedback models with typical variability time-scales of 10–100 Myr. In Section 5, we further discuss the characteristic variability time-scales of feedback models.

4 HALO MASS AND STAR FORMATION PROPERTIES OF GALAXIES

4.1 Halo and stellar masses of star-forming galaxies

Closely related to the main sequence of star-forming galaxies is the cosmic comoving SFRD. Assuming that all galaxies lie on the main-sequence relation, the SFRD can be calculated as

$$\mathrm{SFRD} = \int \mathrm{SFR}_{\mathrm{SFMS}}(M_*) \times \frac{\mathrm{d}n}{\mathrm{d}M_*}\,\mathrm{d}M_*, \quad (2)$$

where n is the comoving number density of galaxies, M_* is the stellar mass and $\mathrm{SFR}_{\mathrm{SFMS}}(M_*)$ is the main-sequence relation. The SFRD is observed to peak at $z \simeq 2$ (Lilly et al. 1996; Madau et al. 1998; Hopkins 2004; Hopkins & Beacom 2006; Labbé et al. 2010; Cucciati et al. 2012), with the physical drivers of the evolution being the build-up of massive haloes and the suppression of star formation by feedback from stellar winds and AGN (Schaye et al. 2010; Vogelsberger et al. 2013; Torrey et al. 2014a).

Fig. 6 shows how galaxies with different stellar masses and halo masses (M_{200}) contribute to the SFRD. This has been computed by summing the contribution to the SFRD from galaxies in equally spaced logarithmic mass-bins from 10^8 to $10^{14.5}\,\mathrm{M}_\odot$. Bins containing seven or fewer galaxies are excluded from the plot in order to avoid bins with very high Poisson noise. The plot also shows how Schechter functions of the form

$$\mathrm{SFRD}(M) \propto \left(\frac{M}{M_{\mathrm{sch}}}\right)^{\alpha} \times \exp\left(-\frac{M}{M_{\mathrm{sch}}}\right), \quad (3)$$

fit to the measurements, where M is either M_{200} or the stellar mass in a halo and M_{sch} and α are free fit parameters. For the fits in terms of halo mass, we exclude haloes outside the range $10^{10}\,\mathrm{M}_\odot < M_{200} < 10^{12.5}\,\mathrm{M}_\odot$, since a Schechter function does not yield a good fit over the entire range of M_{200}-values of the haloes. For fits in terms of stellar mass, all galaxies with $10^8\,\mathrm{M}_\odot < M_* < 10^{12.5}\,\mathrm{M}_\odot$ are included. The actual distributions measured from the Illustris simulation are overall quite well described by the Schechter fits. This is consistent with the observations from Karim et al. (2011), where the distributions of dSFRD/dlog M_* are also well fit by a Schechter function for (at least) $M_* > 10^8\,\mathrm{M}_\odot$. When comparing dSFRD/dlog M_* in Illustris with the observations from Karim et al. (2011), some tensions are visible. At $z = 0.5$, the normalization of this function is too large in Illustris, and at $z = 3$, it is too low. Deviations are, of course, expected, since dSFRD/dlog M_* is closely linked to the SFMS and stellar mass function in Illustris, which both show tensions with observations. At $z = 1$, the figure shows good agreement between Illustris and Karim et al. (2011). This is, however, a coincidence: the SFRs of galaxies are ∼0.5 dex too low in Illustris at this epoch (see Fig. 2), but the normalization of the stellar mass function is too large at low masses. Together, these effects yield a dSFRD/dlog M_* in agreement with observations.

The peak masses of the distributions for dSFRD/dlog M_{200} and dSFRD/dlog M_* are plotted at different redshifts in Fig. 7. At $z \leq 4$, the peaks in the distributions occur at $10^{11.5} < M_{200}/\mathrm{M}_\odot < 10^{12.5}$ and $10^{10.0} < M_*/\mathrm{M}_\odot < 10^{11.0}$. A large contribution of star formation from haloes with $M_{200} = 10^{12}\,\mathrm{M}_\odot$ is, e.g. also seen in the abundance matching analysis of Béthermin et al. (2013).

At $M_{200} \simeq 10^{12}\,\mathrm{M}_\odot$, haloes are most efficient in turning their baryons into stars. This is for example evident when examining M_*/M_{200}, which peaks around $M_{200} \simeq 10^{12}\,\mathrm{M}_\odot$ (this relation is plotted for Illustris in Vogelsberger et al. 2014a and Genel et al. 2014). This is because AGN feedback suppresses the formation of stars in haloes above this characteristic mass, and stellar winds are responsible for suppressing the formation of stars in lower mass haloes. It is therefore not surprising that the peak in dSFRD/dlog M_* is present at $M_{200} \simeq 10^{12}\,\mathrm{M}_\odot$ at $z \lesssim 4$. At $z \gtrsim 4$, there is a decline in the typical masses (both stellar and halo masses) at which stars are formed in Illustris, since haloes and galaxies are less massive at high redshifts.

A feature that is also visible in Fig. 7 is that the mass (both for halo and stellar mass) at which most of the star formation occurs declines from $z = 1$ to 0. This is consistent with the downsizing scenario, where the most-massive galaxies at $z = 0$ have older stellar populations than less-massive galaxies.

4.2 Build-up of stellar components at different halo masses

To study how halo mass affects the average formation history of stars, we create samples of haloes with $M_{200} = 10^{11}$, 10^{12} and $10^{13}\,\mathrm{M}_\odot$. Each sample contains the 100 galaxies with halo masses closest to the mass that defines the samples. Table 1 summarizes the median, minimum and maximum halo mass in each sample. For each galaxy in each sample, we compute the stellar mass growth history by calculating the amount of a galaxy's stellar mass at $z = 0$ that was formed at different lookback times. For this analysis, we include all stars within a halo at $z = 0$, including the stars residing in sub-haloes.

Fig. 8 shows the median stellar growth history for each of the three samples. The galaxies ending up in the most-massive haloes considered (∼$10^{13}\,\mathrm{M}_\odot$) form their stars much earlier than the galaxies ending up in the least-massive haloes. This is most easily seen by comparing the times at which half of the stellar mass present at $z = 0$ is formed (shown as red circles in the figure). It is perhaps not surprising that very-massive haloes form their stars earlier than less-massive ones, since haloes of $10^{12}\,\mathrm{M}_\odot$ contribute most to the global SFR in the Universe, as shown above. However, this trend runs counter to the formation time of the dark matter haloes themselves, where the most-massive haloes form latest as a result of hierarchical structure growth.

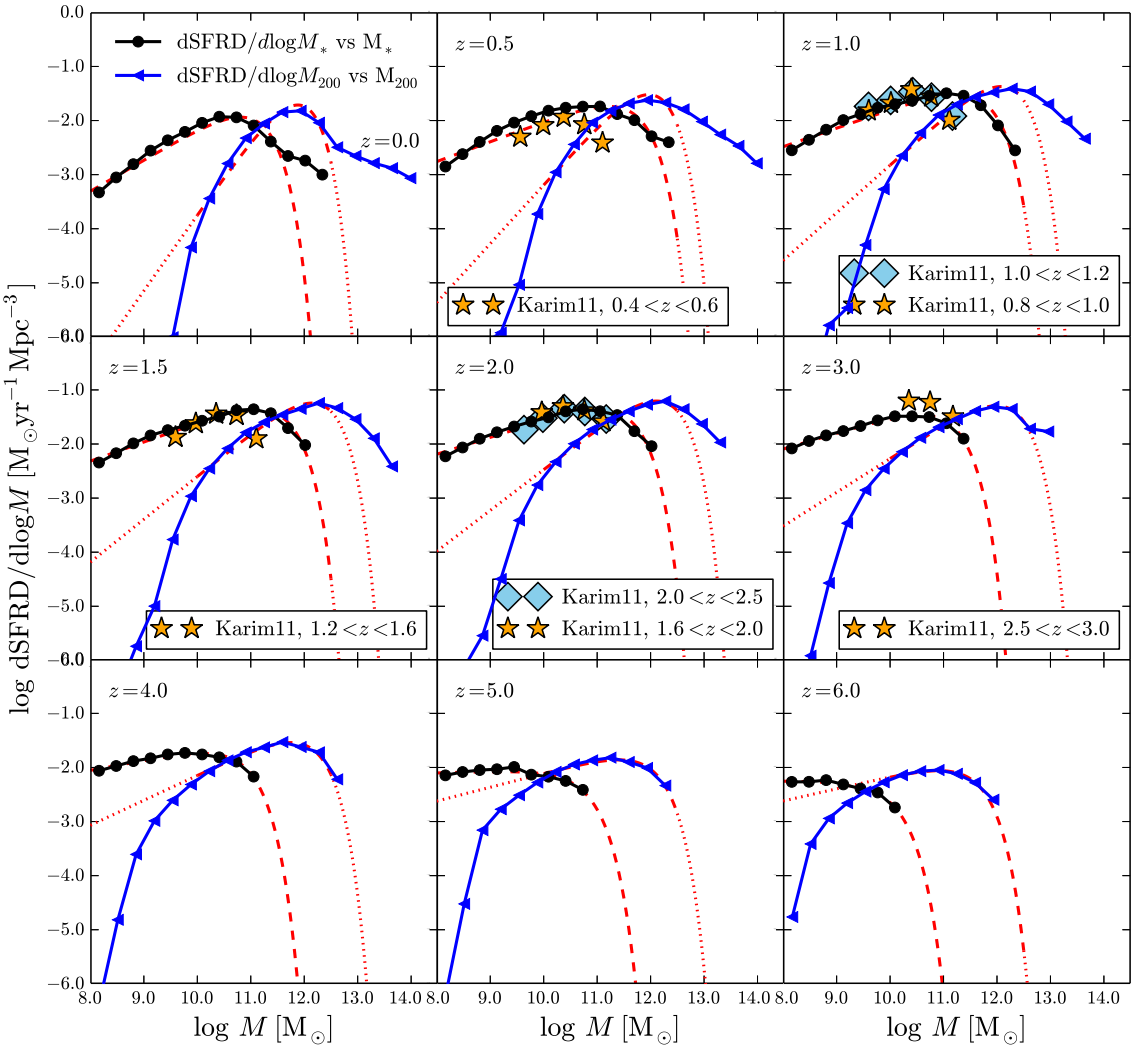

Figure 6. The contribution of haloes with different stellar masses (black circles) and halo masses (blue triangles) to the total SFRD in the Universe at different redshifts. The red dashed lines are Schechter functions of the form of equation (3) fit to the simulation data (outside the fit range the extrapolated Schechter functions are dotted). The distributions evolve with redshift as haloes and galaxies grow. This is also seen in Fig. 7, where evolution of the peak mass is examined. Observations from Karim et al. (2011) are shown as stars or squares.

We compare Illustris to the results from Behroozi et al. (2013b), where the stellar growth history is derived from the stellar mass–halo mass relation ($M_*(M_\mathrm{h}, z)$), which is determined by comparing dark matter merger trees with observations of the cosmic SFR, the SSFR versus M_* and stellar mass functions. For 10^{12} M$_\odot$ haloes, we find excellent agreement between Illustris and Behroozi et al. (2013b). At 10^{11} and 10^{13} M$_\odot$, Illustris predicts stellar components roughly 0.4 dex more massive than Behroozi et al. (2013b). This overproduction of stellar mass in haloes of mass $\sim10^{11}$ and $\sim10^{13}$ M$_\odot$ is essentially independent of redshift. Genel et al. (2014) and Vogelsberger et al. (2014a) found similar deviations between the Illustris simulation and abundance matching results when analysing the high- and low-mass ends of the stellar mass function. Genel et al. (2014) regard these tensions as significant and suggest that more realistic feedback models could potentially help suppress the formation of too-massive stellar components in low- and high-mass galaxies.

5 SFHS OF GALAXIES

5.1 Outliers from the average SFHs

An alternative to studying statistical properties of galaxies with different stellar masses is to analyse their individual SFHs in more detail. To compute the SFH, we select the stars ending up in a galaxy at $z = 0$, and then create a histogram of the initial mass of stars formed in 100 equally spaced bins in terms of lookback time. We include all stars that end up in the main stellar component of a galaxy (i.e. we exclude satellites) when calculating the SFH in this way. We do not distinguish between stars formed *in situ* or *ex situ*. We study galaxies in four different stellar mass ranges at $z = 0$. Three ranges are centred around $M_* = 10^9$, 10^{10} and 10^{11} M$_\odot$, with the widths of the different ranges chosen such that they include 500 galaxies each. We additionally create a range of the 500 galaxies with the most-massive stellar components. Basic properties of the different samples are summarized in Table 2.

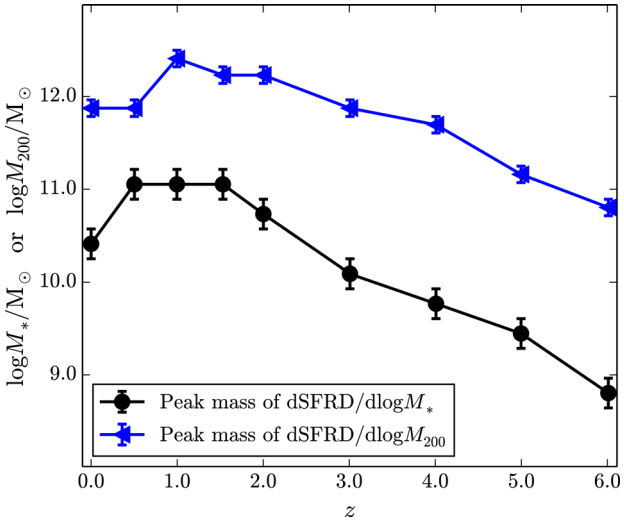

Figure 7. The redshift evolution of the peak stellar mass and halo mass for dSFRD/dlog M_{200} and dSFRD/dlog M_*, respectively, for the distributions in Fig. 6. The peak mass (for both stars and haloes) increases from $z = 6$ to $z \simeq 1$–2, after which it turns over. The error bars are set by the bin width of the histograms shown in Fig. 6.

The mean and median SFHs of the galaxies in the different mass ranges are shown in Fig. 9. For the $10^{11}\,\mathrm{M}_\odot$ range and the 500 most-massive galaxies, the SFH peaks at $z \simeq 2$, and decreases at later epochs. These trends are qualitatively in good agreement with other studies of SFHs of galaxies (Behroozi et al. 2013b; Simha et al. 2014). For the 10^9 and $10^{10}\,\mathrm{M}_\odot$ mass ranges, the peak is significantly broader, and it occurs at $z \simeq 1$. In general, the mean SFR is 10–20 per cent larger than the median value, since the mean is more sensitive to extreme outliers with high SFRs.

Different galaxies experience a variety of gas accretion and merger histories, and they are therefore expected to exhibit diverse SFHs. We illustrate this in Fig. 10, where we show for each mass range the SFR of the galaxies that form 50 per cent of their stellar mass earliest or latest, compared to the average history of the corresponding sample. In all mass ranges, it is possible to find SFHs with early or late star formation. The galaxies with decidedly early SFHs exhibit a similarly bursty epoch at a lookback time of $\simeq$ 10–13 Gyr, and the galaxies with late SFHs display a prominent star-forming mode contributing at $z \lesssim 0.5$ and hardly any high-redshift star formation.

5.2 Modes of star formation in a principal component analysis

The relative similarity seen in Fig. 10 of the galaxies in the tails of the SFH distribution, forming their stars extremely late or early, suggests that a more systematic study of the star formation modes in the Illustris galaxies is worthwhile. As a tool for statistically characterizing the SFHs, we have adopted a *principal component analysis* (PCA; inspired by Cohn & Voort 2015) where the SFH of a galaxy is seen as a vector in a N-dimensional space, where N is the number of bins used to characterize the SFH of a galaxy (we use $N = 100$). A key quantity in a PCA analysis is the average SFH of the galaxies in the sample,

$$\langle \mathrm{SFR} \rangle(t_i) = \frac{1}{N_{\mathrm{galaxies}}} \sum_{j=0}^{N_{\mathrm{galaxies}}-1} \mathrm{SFR}_j(t_i), \tag{4}$$

for $i = 0, \ldots, N-1$. We furthermore define the scatter matrix,

$$C_{mn} = \sum_{j=0}^{N_{\mathrm{galaxies}}-1} \left[\mathrm{SFR}_j(t_m) - \langle \mathrm{SFR} \rangle(t_m)\right] \left[\mathrm{SFR}_j(t_n) - \langle \mathrm{SFR} \rangle(t_n)\right]. \tag{5}$$

Of special interest are the eigenvectors of C_{mn}, which are called the *principal components* (PC_i, for $i = 0, \ldots, N-1$) and describe the deviations between the SFH of individual galaxies and the mean SFH of a sample. Principal components diagonalize the scatter matrix, implying that the scatter between different PC_i's is uncorrelated. Conventionally, the PCs are ordered in descending order by the contribution they make to the total variance. Often, the first components account for much of the variance, and the corresponding eigenvectors can be interpreted in physical terms. In our case, they can serve the purpose of characterizing the most important 'modes' of the SFH.

In terms of the principal components, the SFH of a galaxy can be written as

$$\mathrm{SFR} = \langle \mathrm{SFR} \rangle + \sum_{i=0}^{N-1} q_i \times \mathrm{PC}_i, \tag{6}$$

where q_i is the coefficient determining the strength of the contribution of PC_i for a specific galaxy. Since we have binned our SFHs in $N = 100$ bins, we formally get 100 principal components, and for each of the 500 galaxies in each sample we obtain 100 coefficients q_i. The limited size of our galaxy set means that only the leading PC components are robust against the noise.

Fig. 11 shows the mean SFH for the $M_* = 10^{10}\,\mathrm{M}_\odot$ sample together with the three leading modes, PC_0, PC_1 and PC_2. The PC_0-mode accounts for galaxies forming stars early or late, depending on whether the coefficient q_0 is positive or negative. PC_1 and PC_2 cross the zero-point two and three times, respectively, and they are therefore determining the more detailed evolution of the SFH. In general, PC_i crosses the zero-point $i + 1$ times, and therefore is associated with a physical time-scale of the order of $t_{\mathrm{H}}/(i + 1)$, where $t_{\mathrm{H}} = 13.7$ Gyr is the Hubble time.

For all the four mass samples from Table 2, the PC_0 is plotted in Fig. 12. They all appear similar and have the feature that a positive q_0-value describes a galaxy forming stars earlier than the mean of the sample. The only remarkable difference between the PC_0 eigenvectors from the different samples is that the lookback time where the change from positive to negative contributions occurs shifts to higher values for the more-massive galaxies. The trend that massive galaxies have earlier bursty epochs than less-massive

Table 1. Three samples with different haloes masses, M_{200}. Each sample includes the 100 galaxies with masses closest to 10^{11}, 10^{12} and $10^{13}\,\mathrm{M}_\odot$ at $z = 0$.

$M_{200}/\mathrm{M}_\odot$	median(M_{200})/$\mathrm{M}_\odot$	min (M_{200})/median(M_{200})	max (M_{200})/median(M_{200})	N_{galaxies}
10^{11}	10^{11}	1.00	1.00	100
10^{12}	10^{12}	0.97	1.03	100
10^{13}	9.2×10^{12}	0.77	1.42	100

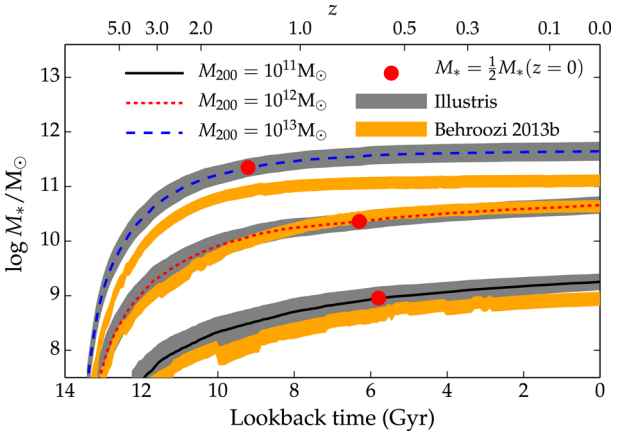

Figure 8. The fraction of the current stellar mass formed as function of lookback time for galaxies residing in haloes with M_{200}-values of 10^{11}, 10^{12} and $10^{13}\,\mathrm{M}_\odot$ (see details about samples in Table 1). The grey shaded regions correspond to 1σ scatter in each mass range. The orange regions are the 1σ confidence intervals from the abundance matching of Behroozi et al. (2013b) for $M_{200}/\mathrm{M}_\odot = 10^{11}$, 10^{12} and $10^{13}\,\mathrm{M}_\odot$.

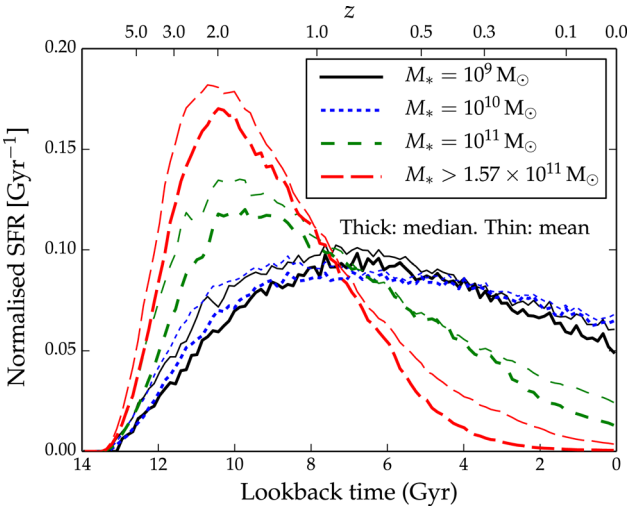

Figure 9. Mean and median (thin and thick lines, respectively) SFHs of galaxies in the four different stellar mass ranges (see Table 2). The SFRs are normalized so that $\int \mathrm{SFR}(t)\mathrm{d}t = 1$.

galaxies is therefore both reflected by the mean SFH and a zeroth principal component that peaks at higher redshift.

Fig. 13 compares the actual SFHs for a selection of galaxies to the mean SFH of the $M_* = 10^{10}\,\mathrm{M}_\odot$ sample, and the SFHs reconstructed by including only PC_0 and by including both PC_0 and PC_1. By including PC_0, it is possible to capture whether a galaxy forms its stars early or late. Including the PC_1 mode as well gives of course a better fit to the actual SFH of the galaxies. Components 0 and 1 account for 33 per cent and 10 per cent of the total scatter in the sample. These percentages indicate that while a given galaxy's SFH can already be described reasonably well by just PC_0 and PC_1, variability on time-scales much shorter than described by them needs to be considered for an accurate description.

We note that it could potentially be useful to construct a family of SFHs based on a combination of the mean SFH for the Illustris galaxies and one or more of the principal components from the PCA analysis. An attractive property of a model based on the mean SFH and the leading principal component would be that it could describe a realistic SFH of a galaxy with only one free parameter (the relative contribution of the mean SFH and the leading principal component). Such a model would be more physically motivated than e.g. single-burst models or τ-models, which are often used when fitting spectral energy distributions of galaxies. In future work, we will construct such a model and show how it can be used for fitting spectral energy distributions. Such an approach could yield significant advantages because the accuracy and robustness of spectral energy distribution modelling can be very sensitive to the assumed SFH (e.g. Michałowski et al. 2012, 2014; Torrey et al. 2014b; Hayward & Smith 2015).

5.3 Assessing the SFH variability time-scale

As each principal component has an associated time-scale, the PCA analysis may also be used to characterize variability of the SFHs, which in turn is influenced by the adopted physical model for feedback processes and the ISM. In Fig. 14, we show the cumulative fraction of the variance accounted for as a function of the number of principal components included. The two most-massive samples behave similarly for the low- and high-resolution run. For the two low-mass bins, the difference between the low- and high-resolution run is larger. To quantitatively measure how well-converged the cumulative fractions in Fig. 14 are, we use the difference in the fraction of the scatter accounted for by the 25 first components in the low- and high-resolution run. For the various bins, the differences are 21, 11, 3 and 1 per cent (from lowest to highest mass). The two most-massive ranges are therefore well converged, unlike the two least-massive ranges, where some of the scatter comes from Poisson noise. This is also consistent with Fig. 9, where the mean and median SFH of the low-massive range seem to be more affected by noise the most-massive range.

The time-scale at which 95 per cent of the scatter is accounted for is 500 Myr in the two most-massive bins, and for the other mass ranges this time-scale is smaller, which might be a consequence of the contribution of Poisson noise being more important

Table 2. Four different samples of galaxies in different stellar mass ranges. The first three samples include the 500 galaxies with stellar masses (M_*) closest to 10^9, 10^{10} and $10^{11}\,\mathrm{M}_\odot$ at $z = 0$. The fourth range includes the 500 galaxies with the largest stellar masses at $z = 0$. The median, minimum and maximum stellar mass for each sample is also listed.

$M_*/\mathrm{M}_\odot$	median(M_*)/$\mathrm{M}_\odot$	min (M_*)/median(M_*)	max (M_*)/median(M_*)	N_{galaxies}
10^9	1.0×10^9	0.99	1.02	500
10^{10}	1.0×10^{10}	0.95	1.05	500
10^{11}	9.4×10^{10}	0.83	1.30	500
$>1.57 \times 10^{11}$ (most massive)	2.6×10^{11}	0.60	12.70	500

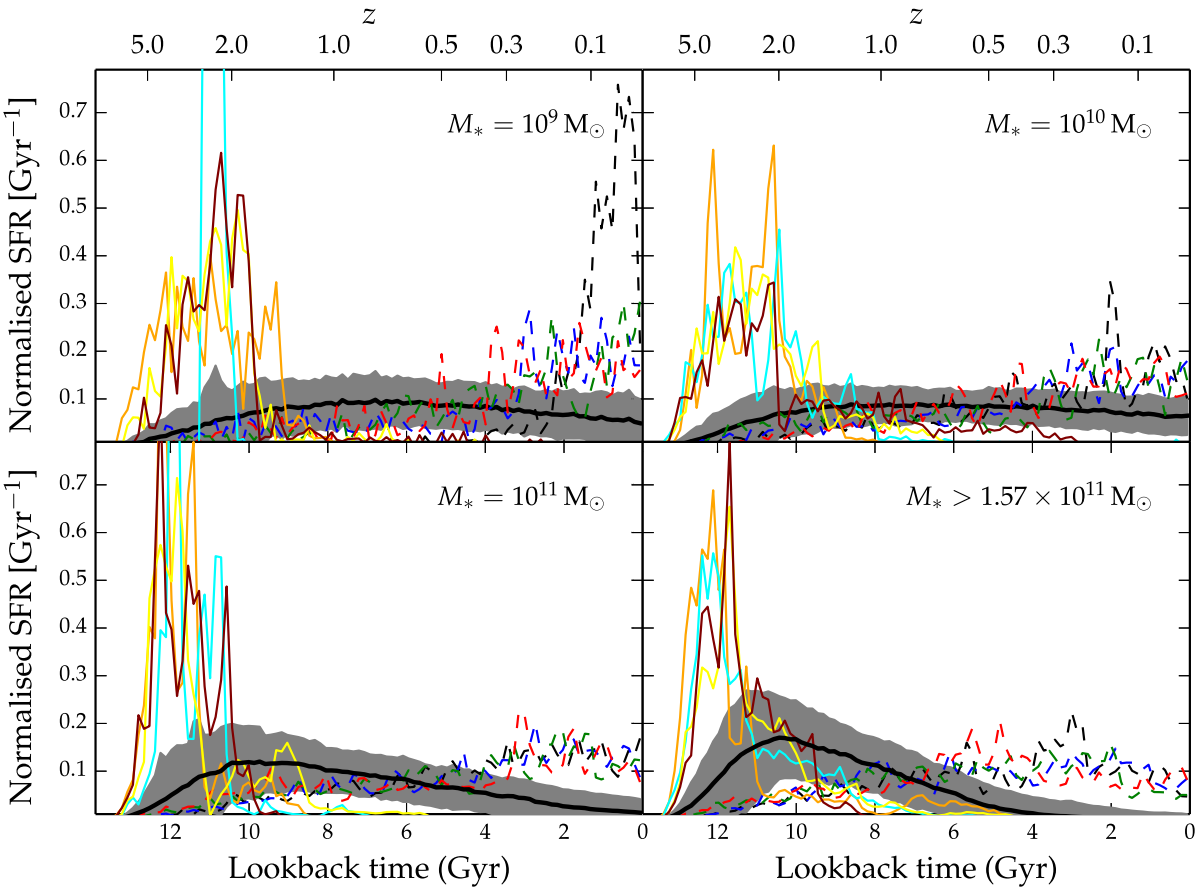

Figure 10. For each M_*-range, we have selected the four galaxies that form 50 per cent of their stars earliest or latest (solid and dashed thin lines, respectively). The median profiles for each range are shown by the thick black lines, and the 68 per cent confidence intervals are the shaded regions. The normalization convention is $\int \mathrm{SFR}(t)\mathrm{d}t = 1$.

in the low-massive galaxies, where there are fewer star particles per time bin. Based on the variability time-scale of the most-massive range, the characteristic time-scale for fluctuations in the galactic star formation for the ISM model adopted in Illustris has characteristic time-scale of 500 Myr. In Section 3.3, we saw that the scatter in the SFMS decreased significantly (by 0.05 dex), when the SFH was smoothed on this time-scale, and that the decrease in the scatter was more moderate when smoothing over shorter time-scales.

We note that there exist other simulation feedback models which show variability time-scales an order of magnitude lower than Illustris. Hopkins et al. (2014), for example, include a treatment of radiative feedback from young stars and more localized supernova feedback in giant molecular clouds. Another model with a short variability time-scale is Governato et al. (2014), where this is achieved through a high star formation threshold and delayed radiative cooling. Interestingly, variability itself could be used as an important constraint of feedback models, although the fact that highly variable feedback models will induce differences between SFR indicators may make this complicated in practice.

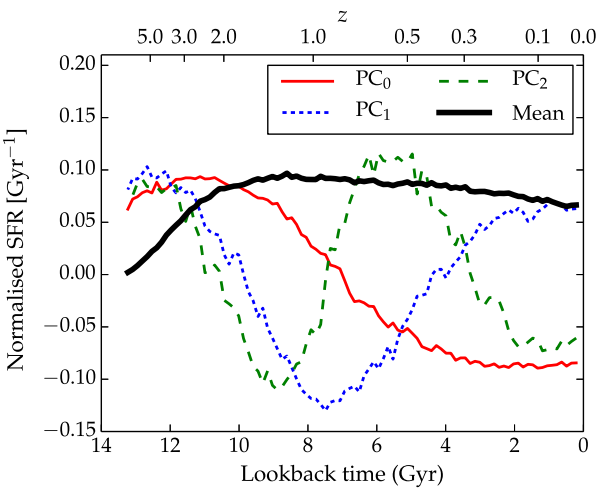

Figure 11. The mean SFR for the sample with $M_* = 10^{10}\,\mathrm{M}_\odot$ (from Table 2) together with the first three principal components (PC$_i$ for $i = 0$, 1, 2) describing the scatter around the mean. The normalizations of the principal components are arbitrary.

5.4 Relations between the SFH main mode and galaxy properties

We have previously shown that the q_0-value of the PCA-decomposed SFH of a galaxy captures whether its stellar population forms early or late. We therefore expect correlations between q_0 and other quantities sensitive to the age of stellar populations. Fig. 15 shows how q_0 for the different galaxy mass bins relates to the lookback time when half of the stellar mass is formed (T_{50}), the $g - r$

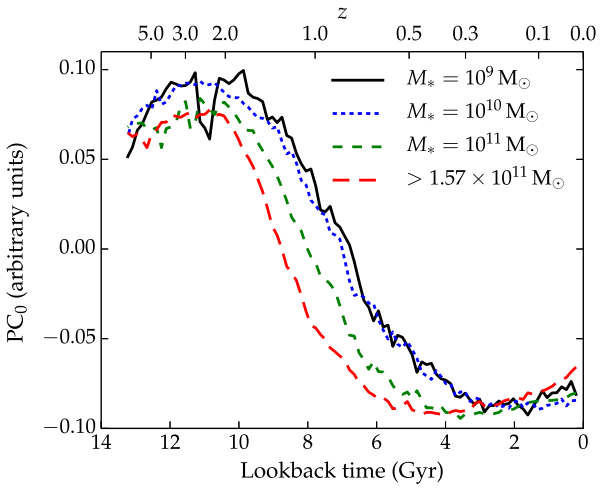

Figure 12. The zeroth principal component for the four different mass samples in Table 2. In all mass samples, the PC_0 component is of similar shape and shows a positive contribution at a lookback time of 11 Gyr, and a negative contribution at lookback times smaller than $\simeq 7$ Gyr.

colour at $z = 0$, the black hole mass at $z = 0$, and the dark matter mass (friends-of-friends) at $z = 0$. q_0 correlates strongly with T_{50}, which is in agreement with the SFHs in Fig. 13. There is an offset between the normalization of this correlation between the different samples. This is partially because the most-massive galaxies form their stars before the least-massive galaxies (see also Fig. 9).

The correlation between q_0 and $g - r$ is also expected, since old stellar populations are expected to be redder than younger stellar populations. In all the samples, there is an extended distribution of the $g - r$ colour, which splits the galaxies into red galaxies (with high values of $g - r$) with large q_0-values and blue galaxies (low values of $g - r$) with lower q_0-values. The division between the blue and red galaxy populations is for example seen for the most-massive galaxies, where the red galaxies have $g - r \gtrsim 0.65$. For the sample containing the most-massive galaxies, there is a larger fraction of red galaxies than for the samples of less-massive galaxies, where the blue population dominates.

The presence of a red and blue population of galaxies that form their stars late and early, respectively, is consistent with the *red and blue cloud*, which are connected through the *green valley*, established from observations of galaxies (e.g. Strateva et al. 2001; Faber et al. 2007; Bowler et al. 2014; Schawinski et al. 2014). Galaxies in the blue cloud are known to be actively star-forming, whereas the red cloud consists of passive galaxies that are most likely quenched by feedback processes. In Illustris, there is a correlation between the SFH and the black hole mass at $z = 0$ for the three most-massive bins (*lower-left panel*, Fig. 15), which suggests that the galaxies that form their stars early are quenched by AGN feedback, although other interpretations of the correlation cannot be ruled out by the analysis presented here. For the $10^9\,M_\odot$ galaxies, such a trend is not evident in the simulation, which is expected because the black

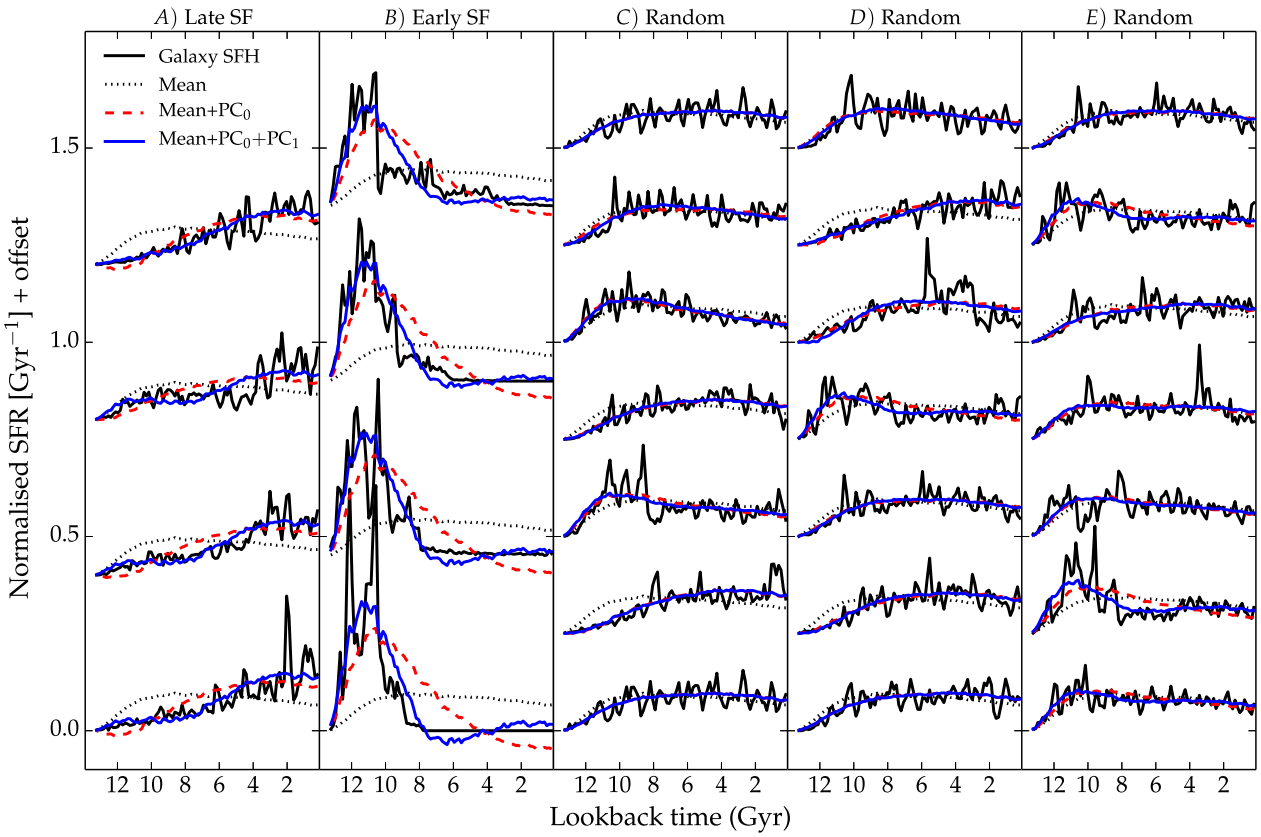

Figure 13. SFHs of individual galaxies (black lines) and the mean profile for the sample of galaxies with $M_* = 10^{10}\,M_\odot$ (grey dashed lines). Also shown are profiles including the contribution from the zeroth principal component (red dashed line) and components 0 and 1 (blue line). Panels A and B show eight galaxies that form their stars late and early, respectively (the same profiles are shown in Fig. 10). Panels C, D and E show 21 randomly selected galaxies from the sample with $M_* = 10^{10}\,M_\odot$.

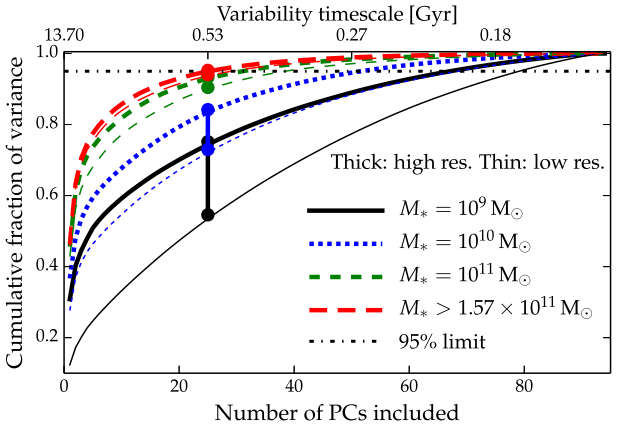

Figure 14. The cumulative fraction of the total variance in the SFHs accounted for as a function of the number of principal components that are included. The thick lines show the full-resolution run and the thin lines show the low-resolution run. The vertical lines (connected by circles) measure how well-converged the variability time-scale is for the different mass ranges.

hole feedback models in Illustris do not significantly affect galaxies in this mass range.

The panel that shows the dark matter halo mass, $M_{\rm halo}$, at $z = 0$ versus q_0 reveals that these two variables are correlated for the samples with the two highest stellar masses. Furthermore, galaxies that form their stars late (low q_0) have halo masses that are close to $10^{12}\,{\rm M}_\odot$, whereas galaxies that form stars early have higher halo masses. This is expected within the framework in which stars are most likely to form in haloes of mass $10^{12}\,{\rm M}_\odot$. For the samples with $M_* = 10^9$ and $10^{10}\,{\rm M}_\odot$, a weak anticorrelation between q_0 and $M_{\rm halo}$ is present. The anticorrelation most likely arises because a halo mass of $10^{12}\,{\rm M}_\odot$ is never reached for these galaxies, so they form stars most efficiently at low redshift, when the dark matter halo mass is as close as possible to $10^{12}\,{\rm M}_\odot$.

6 WHAT PROCESSES CONTRIBUTE TO THE SCATTER IN THE SFMS?

After having studied the halo growth and SFHs of individual galaxies, we will now return to the topic of the scatter in the SFMS. In Section 3.3, we showed that the scatter decreased from 0.27 to 0.22 dex when calculating the scatter from a 500-Myr-averaged SFR instead of the instantaneous SFR. The scatter in the SFR over time-scales of less than 500 Myr is therefore $\simeq$0.16 dex (computed as $\sqrt{0.27^2 - 0.22^2}$). This allows distinguishing between scatter induced by short-time-scale variations (<500 Myr) and long-time-scale variations (>500 Myr), where the latter mode is dominant in Illustris.

In Section 5.4, we showed that the principal component, q_0, of a galaxy's SFH correlates (or is anticorrelated) with the dark matter halo mass, the black hole mass and the galaxy colour. In Fig. 16, we show how these quantities behave for galaxies above and below

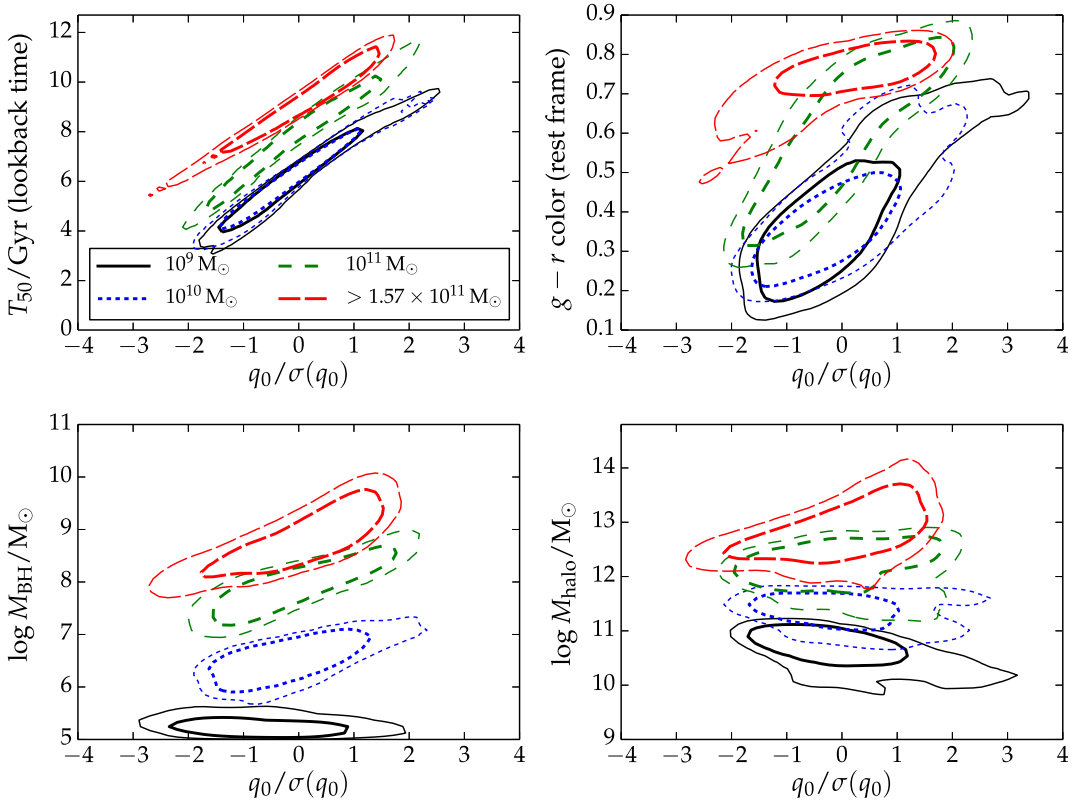

Figure 15. The dependence of various galaxy properties on the coefficient describing the contribution from the zeroth principal component (q_0). The thick and thin contours show 68 and 90 per cent confidence intervals, respectively, for the galaxies in the samples with stellar masses of $M_*/{\rm M}_\odot = 10^9$, 10^{10}, 10^{11}, as well as for the 500 most-massive galaxies. The upper-left panel shows that the lookback time at which 50 per cent of the stars in a galaxy is formed (T_{50}) correlates strongly with q_0. There also exists correlations with the $g - r$ colour (upper-right panel), and the black hole mass at $z = 0$ (lower-left panel). For the two most-massive stellar mass samples, q_0 correlates with the dark matter halo mass. For the two samples with the least-massive galaxies, an anticorrelation is observed (lower-right panel). q_0 is normalized by the standard deviation of this parameter for the 500 galaxies in each sample.

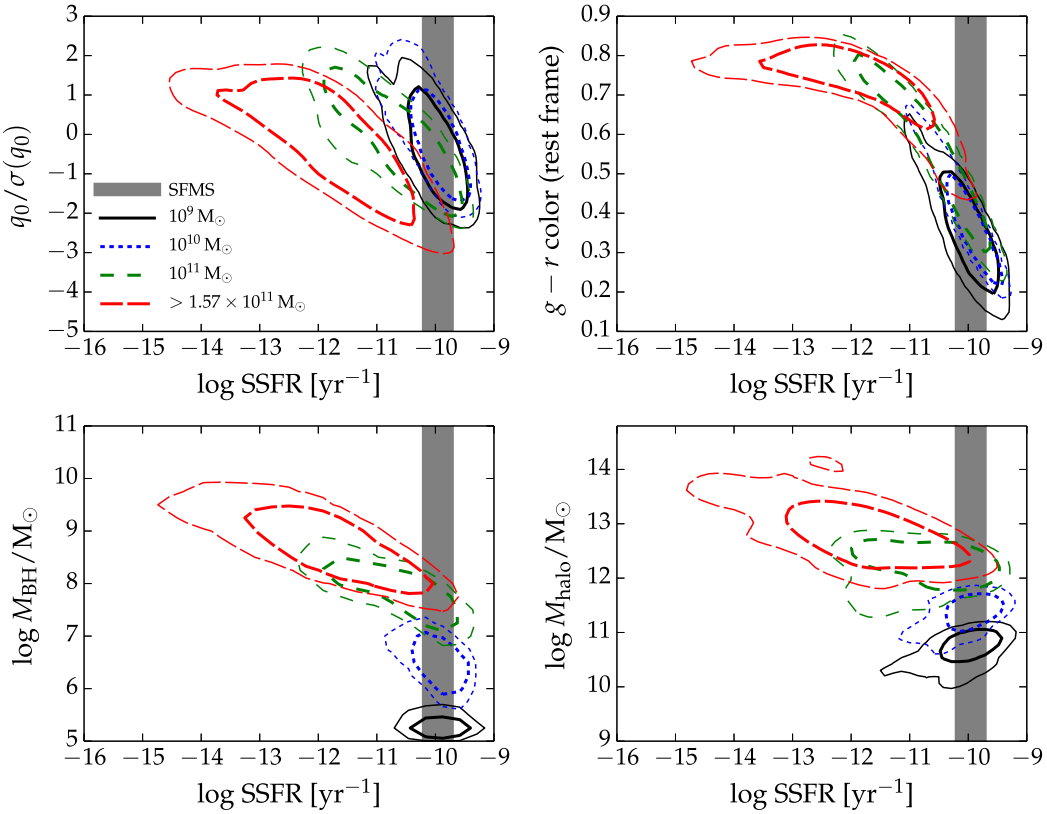

Figure 16. This figure shows how various physical quantities behave across the SFMS, which is shown as a grey shaded area (it indicates the median SSFR $\pm 1\sigma$). The confidence intervals and the various physical quantities are the same as in Fig. 15. The correlations and anticorrelations in the figure show that the spread in SFHs (quantified with q_0), dark matter halo masses and black hole masses likely are responsible for producing scatter in the SFMS .

the SFMS in different mass bins (we again use the stellar mass bins from Table 2). Essentially, all galaxies with an SSFR enhanced more than 1σ above the SFMS have negative q_0 values, which implies that they formed their stars later than typical galaxies of the same stellar mass. The galaxies that are 1σ or more below the SFMS in the two low-mass bins all have positive q_0, which implies that these galaxies formed their stars in the early Universe. Taking these considerations into account, it is not surprising that galaxies above the SFMS have bluer $g - r$ colours than galaxies below it.

The decline of black hole mass with SSFR also shows that black hole quenching could be an important mechanism for determining whether a galaxy is in the upper or lower part of the main sequence. Differences in dark matter halo masses among different galaxies also produce scatter in the SFMS, since galaxies with $M_{\rm halo} \simeq 10^{12}\,{\rm M}_\odot$ (where gas is turned most efficiently into stars) tend to have elevated SSFRs. The halo mass is mainly determined by the long-time-scale evolution of a galaxy (i.e. it is relatively insensitive to baryonic processes), so the halo evolution mainly contributes to the long-time-scale variation (>500 Myr) of a galaxy's SFH. The short-time-scale variability is likely due to short-time-scale variability in the stellar feedback, gas accretion and black hole activity.

7 DISCUSSION

7.1 The normalization of the SFMS

In Section 3, we demonstrated that in Illustris, star-forming galaxies exhibit a tight, approximately linear correlation between the SFR and stellar mass, as is observed for real galaxies. Although the normalization agrees well with observations at $z = 0$ and 4, the normalization in Illustris is less than that observed for intermediate redshifts $z \sim 1$–2. A similar problem of underpredicting the normalization of the main-sequence relation at $z \simeq 2$ has previously been noted by several authors (e.g. Daddi et al. 2007; Davé 2008; Damen et al. 2009), and it appears to be a generic problem for cosmological hydrodynamical simulations and semi-analytical models. Thus, it is worthwhile to consider potential solutions to this problem and discuss whether it is indeed a serious problem.

7.1.1 *Potential theoretical solutions*

In Illustris and other cosmological hydrodynamical simulations, the SFR–stellar mass relation is a result of the correlation of gas inflow and outflow rates with halo mass (e.g. Davé et al. 2011, 2012; Dekel et al. 2013). Thus, inaccurate gas net accretion rates would lead to an incorrect normalization of the SFR–stellar mass relation. Damen et al. (2009) compared the growth rate of galaxies in observations with semi-analytical models (Guo & White 2008) and argued that a time-varying IMF cannot resolve the issue of too low normalizations at $1 \lesssim z \lesssim 2$. Instead, Damen et al. suggest that the discrepancy may be due to the simplified schemes for gas accretion used in semi-analytical models. Mitchell et al. (2014) identified the same problem of a too low normalization of the main sequence at $z = 2$ in semi-analytical models. They showed that a modification of the time-scale over which gas ejected by feedback is reincorporated into galaxies can help to fix this problem for galaxies with $M_* \lesssim 10^{10}\,{\rm M}_\odot$ (a modification of the reincorporation

time-scale was also studied by Henriques et al. 2013), but it cannot solve the problem for more-massive galaxies.

Concerns regarding gas inflow rates are less applicable to the Illustris simulation than to semi-analytical models because in Illustris gas accretion is explicitly treated using an accurate hydrodynamics algorithm (e.g. Bauer & Springel 2012; Kereš et al. 2012; Sijacki et al. 2012; Vogelsberger et al. 2012). Still, it is possible that the gas cooling rates in Illustris are systematically offset. For example, if the phase structure or metal content of the hot halo gas is incorrect, gas inflow rates could end up being inaccurate (Nelson et al. 2013; Hayward et al. 2014a).

Outflows are also important for setting the normalization of the SFR–stellar mass relation, but they must still be treated with sub-resolution models even in state-of-the-art large-volume cosmological hydrodynamical simulations. One can easily imagine altering the normalization of the SFR–stellar mass relation by e.g. modifying the mass-loading factor of stellar winds. However, the parameters of the sub-resolution feedback models used in Illustris were determined by requiring the simulation to match observations such as the $z = 0$ stellar mass function. Thus far, attempts to tune the parameters to reconcile the discrepancy with which we are concerned here without breaking these constraints were unsuccessful (Torrey et al. 2014a). Nevertheless, this does not preclude the possibility of solving the discrepancy through the use of more sophisticated feedback models.

The EAGLE simulation (Schaye et al. 2015) is a large-scale cosmological galaxy formation simulation with a feedback model different from the one used in Illustris. A feature of the model in EAGLE is that the wind velocity is untied from the local dark matter velocity dispersion. The EAGLE simulation also has a too-low normalization of the SFMS at $z = 1$–2 (Furlong et al. 2014). They suggest that a burstier star formation model can help solve this problem. The idea is that the SSFR of star-forming galaxies can shift to larger values if galaxies typically form their stars at higher SFRs. However, this requires that galaxies increase the time they spend being passive (i.e. below the SFMS). This suggestion is in good agreement with our finding in Section 3 that the SFR has to be further decoupled from dark matter accretion rate in order to produce the correct normalization of the SFMS at $z = 2$. Examples of burstier feedback models are presented in Hopkins et al. (2014) and Governato et al. (2010).

7.2 The paucity of starbursts in Illustris

The small number of strong starbursts (i.e. galaxies that lie significantly above the SFMS) identified in Illustris is another discrepancy in addition to the disagreement in the normalization of the SFR–stellar mass relation discussed above. As shown in Fig. 4, at all redshifts considered, 2.5σ outliers from the SFR–stellar mass relation contribute at most a few per cent of the total SFRD in massive galaxies ($M_* \gtrsim 10^{10}\,\mathrm{M}_\odot$), and this contribution is a factor of at least a few less than what is inferred from observations. Furthermore, by combining scalings derived from idealized merger simulations with a semi-empirical model, Hopkins et al. (2010) estimated that at all redshifts, merger-induced starbursts account for ∼5–10 per cent of the SFRD of the Universe, which is also at odds with the Illustris results.

One possible reason for the relative shortage of starbursts in Illustris is its kiloparsec-scale spatial resolution. Although the comparison of the low- and high-resolution runs presented in Fig. 4 suggests that the fraction of starbursts is converged, it is possible that this conclusion will change if the resolution is increased significantly, as is often done using zoom-in simulations of galaxies (e.g. Guedes et al. 2011; Marinacci, Pakmor & Springel 2014). It is for example possible that the spatial resolution in both the high- and low-resolution Illustris runs is insufficient to resolve the tidal torques that drive starbursts in mergers. Indeed, the compact sizes (of the order of 100 pc) of the starbursting regions in local ULIRGs (e.g. Sakamoto et al. 2008; Engel et al. 2011) support this interpretation. Furthermore, examination of the individual SFHs presented in Fig. 10 indicates that the galaxies' star formation was burstier at high redshift ($z \gtrsim 2$). Because a fixed comoving softening yields finer resolution at higher redshifts, this observation may also indicate that resolution is the reason for the lack of starbursts in Illustris.

The relatively stiff equation of state of the Springel & Hernquist (2003) sub-resolution ISM model may also serve to suppress starbursts in Illustris. However, in higher resolution idealized merger simulations that employed the same ISM model, SFR elevations of an order of magnitude or more have been found (e.g. Cox et al. 2008; Hayward et al. 2011, 2014a; Torrey et al. 2012). Furthermore, the resulting SFR elevations are sufficient to match the observed interaction induced SFRs of close-pair galaxies in SDSS (Scudder et al. 2012; Patton et al. 2013). We note however that galaxy merger simulations with much softer equations of state show still stronger (albeit shorter) SFR increases (e.g. Mihos & Hernquist 1996). Also, the elevation depends sensitively on the mass ratio and orbital parameters of the merger (e.g. Di Matteo et al. 2007, 2008; Cox et al. 2008). Thus, the sub-resolution ISM model may contribute to the suppression of merger-driven starbursts in Illustris but is unlikely to be the sole reason. But mergers are not the only mechanism that can drive starbursts: it has been suggested that violent disc instability is also an important channel for driving starbursts (e.g. Dekel, Sari & Ceverino 2009b; Ceverino, Dekel & Bournaud 2010; Cacciato, Dekel & Genel 2012; Porter et al. 2014). Such events may be suppressed in Illustris because of the sub-resolution ISM model.

Finally, it is possible that the IR luminosity-inferred SFRs of extreme outliers from the main sequence are overestimates of the true SFR. For highly obscured galaxies, at the peak of the starburst, simulations suggest that older stellar populations (Hayward et al. 2014b) and obscured AGN (Rosenthal et al., in preparation) may contribute to the IR luminosity and thus cause the SFR to be overestimated by a factor of a few. These effects are almost certainly not significant for the bulk of the star-forming galaxy population and thus should not affect the normalization of the SFR–stellar mass relation, but, if they are relevant for any real galaxies, it will likely be those galaxies that are well above the galaxy main sequence. Consequently, these effects may explain the tension between observations and Illustris demonstrated in Section 3.2.

8 CONCLUSIONS

In this work, we have examined the SFMS and individual SFHs of galaxies in the Illustris simulation. Our main findings can be summarized as follows.

(i) The normalization of the SFMS is consistent with the observations at $z = 0$ and 4. At intermediate redshifts, $z \sim 2$, the normalization is significantly lower than reported in observations. There is also a slight tension between the slope of the SFMS for low-mass galaxies, for which Illustris predicts an approximately mass-independent SSFR, whereas observations indicate that the SSFR is a decreasing function of stellar mass. We speculate that more-sophisticated feedback models are required in order to properly recover the observed slope and normalization of the SFMS.

(ii) The scatter in the SFMS in Illustris is $\simeq 0.27$ dex, which is consistent with observations. Most of the scatter, 0.22 dex, comes from long-time-scale ($\gtrsim 500$ Myr) variability effects; this scatter is likely driven by differences in dark matter accretion histories of galaxies of a given stellar mass, which can affect the resulting SFR in multiple ways. A scatter of 0.16 dex originates from variations on time-scales shorter than 500 Myr. This short-time-scale variation is likely driven by short-time-scale variations in the gas accretion rate and stellar and black hole feedback.

(iii) The highest star formation efficiency is found in haloes with masses of 10^{12} $M_\odot$, and the largest contribution to the SFRD comes from galaxies in haloes with masses of $10^{11.5}$–$10^{12.5}$ $M_\odot$ at $z \lesssim 4$. At higher redshift, the dominant contribution originates in less-massive haloes because of the declining abundance of haloes with high masses. The stellar masses of the galaxies contributing most strongly to the global SFRD lie in the range 10^{10}–10^{11} $M_\odot$, which is in agreement with observational constraints on this peak mass. Another result is that galaxies with stellar masses above $\simeq 10^{11}$ $M_\odot$ that reside in $\sim 10^{12}$ $M_\odot$ haloes form their stars later than galaxies in more-massive haloes. This is a consequence of star formation being most efficient in $\sim 10^{12}$ $M_\odot$ haloes.

(iv) We have studied the dominant modes and the time variability of individual SFHs with a PCA, finding that the characteristic time-scale of star formation fluctuations in the simulation is 500 Myr. Another result of this principal component analysis is that many features of a galaxy's SFH can be described by the leading principal component. This leads us to suggest that SFHs based on one or several principal components can be useful when fitting the spectral energy distribution of observed galaxies.

(v) Compared to observations, there is a paucity of strong starbursts in Illustris, as evidenced by the small number of galaxies that lie significantly above the SFMS. This is likely caused in part by a lack of spatial resolution in the cosmological simulation, but it may also reflect the relatively stiff equation of state model used in Illustris' sub-grid model for the regulation of star formation in the ISM.

In future cosmological simulations of galaxy formation, the relative frequency of starbursts may well turn out to be an important constraint that informs about adequate models for the ISM. In Illustris, starbursts are presumably damped in intensity and stretched in time by the stiff ISM model, without much affecting the stellar mass and the structural properties of merger remnants. If a significant number of starbursts are triggered by disc instabilities, which are suppressed by the ISM model used in Illustris, the resulting discrepancies could potentially be more significant. Refined simulation models will be necessary to clarify this question.

ACKNOWLEDGEMENTS

We thank Sune Toft, Peter Behroozi, Nicholas Lee and David Sanders for useful discussions. The Dark Cosmology Centre is funded by the Danish National Research Foundation. CCH is grateful to the Klaus Tschira Foundation and the Gordon and Betty Moore Foundation for financial support. VS acknowledges support by the European Research Council under ERC-StG EXAGAL-308037.

REFERENCES

Atek H. et al., 2014, ApJ, 789, 96
Bauer A., Springel V., 2012, MNRAS, 423, 2558
Behroozi P. S., Wechsler R. H., Conroy C., 2013a, ApJ, 762, L31
Behroozi P. S., Wechsler R. H., Conroy C., 2013b, ApJ, 770, 57
Béthermin M. et al., 2012, ApJ, 757, L23
Béthermin M., Wang L., Doré O., Lagache G., Sargent M., Daddi E., Cousin M., Aussel H., 2013, A&A, 557, A66
Bird S., Vogelsberger M., Haehnelt M., Sijacki D., Genel S., Torrey P., Springel V., Hernquist L., 2014, MNRAS, 445, 2313
Bouché N. et al., 2010, ApJ, 718, 1001
Bowler R. A. A. et al., 2014, MNRAS, 440, 2810
Brinchmann J., Charlot S., White S. D. M., Tremonti C., Kauffmann G., Heckman T., Brinkmann J., 2004, MNRAS, 351, 1151
Cacciato M., Dekel A., Genel S., 2012, MNRAS, 421, 818
Cemile Marsan Z. et al., 2014, preprint (arXiv:1406.0002)
Ceverino D., Dekel A., Bournaud F., 2010, MNRAS, 404, 2151
Chabrier G., 2003, PASP, 115, 763
Cohn J. D., Voort F. v. d., 2015, MNRAS, 446, 3253
Cox T. J., Jonsson P., Somerville R. S., Primack J. R., Dekel A., 2008, MNRAS, 384, 386
Cucciati O. et al., 2012, A&A, 539, A31
Daddi E. et al., 2007, ApJ, 670, 156
Daddi E. et al., 2010, ApJ, 714, L118
Damen M., Förster Schreiber N. M., Franx M., Labbé I., Toft S., van Dokkum P. G., Wuyts S., 2009, ApJ, 705, 617
Davé R., 2008, MNRAS, 385, 147
Davé R., Oppenheimer B. D., Finlator K., 2011, MNRAS, 415, 11
Davé R., Finlator K., Oppenheimer B. D., 2012, MNRAS, 421, 98
Dekel A., Mandelker N., 2014, MNRAS, 444, 2071
Dekel A. et al., 2009a, Nature, 457, 451
Dekel A., Sari R., Ceverino D., 2009b, ApJ, 703, 785
Dekel A., Zolotov A., Tweed D., Cacciato M., Ceverino D., Primack J. R., 2013, MNRAS, 435, 999
Di Matteo P., Combes F., Melchior A.-L., Semelin B., 2007, A&A, 468, 61
Di Matteo P., Bournaud F., Martig M., Combes F., Melchior A.-L., Semelin B., 2008, A&A, 492, 31
Diemand J., Kuhlen M., Madau P., Zemp M., Moore B., Potter D., Stadel J., 2008, Nature, 454, 735
Dressler A., 1980, ApJ, 236, 351
Dutton A. A., van den Bosch F. C., Dekel A., 2010, MNRAS, 405, 1690
Elbaz D. et al., 2011, A&A, 533, A119
Engel H., Davies R. I., Genzel R., Tacconi L. J., Sturm E., Downes D., 2011, ApJ, 729, 58
Faber S. M., Jackson R. E., 1976, ApJ, 204, 668
Faber S. M. et al., 2007, ApJ, 665, 265
Furlong M. et al., 2014, preprint (arXiv:1410.3485)
Genel S., Vogelsberger M., Nelson D., Sijacki D., Springel V., Hernquist L., 2013, MNRAS, 435, 1426
Genel S. et al., 2014, MNRAS, 445, 175
Genzel R. et al., 2010, MNRAS, 407, 2091
Governato F. et al., 2010, Nature, 463, 203
Governato F. et al., 2014, preprint (arXiv:1407.0022)
Guedes J., Callegari S., Madau P., Mayer L., 2011, ApJ, 742, 76
Guo Q., White S. D. M., 2008, MNRAS, 384, 2
Hayward C. C., Smith D. J. B., 2015, MNRAS, 446, 1512
Hayward C. C., Kereš D., Jonsson P., Narayanan D., Cox T. J., Hernquist L., 2011, ApJ, 743, 159
Hayward C. C., Jonsson P., Kereš D., Magnelli B., Hernquist L., Cox T. J., 2012, MNRAS, 424, 951
Hayward C. C., Torrey P., Springel V., Hernquist L., Vogelsberger M., 2014a, MNRAS, 442, 1992
Hayward C. C. et al., 2014b, MNRAS, 445, 1598
Henriques B. M. B., White S. D. M., Thomas P. A., Angulo R. E., Guo Q., Lemson G., Springel V., 2013, MNRAS, 431, 3373
Hinshaw G. et al., 2013, ApJS, 208, 19
Hopkins A. M., 2004, ApJ, 615, 209
Hopkins A. M., Beacom J. F., 2006, ApJ, 651, 142
Hopkins P. F., Younger J. D., Hayward C. C., Narayanan D., Hernquist L., 2010, MNRAS, 402, 1693

Hopkins P. F., Kereš D., Oñorbe J., Faucher-Giguère C.-A., Quataert E., Murray N., Bullock J. S., 2014, MNRAS, 445, 581
Hubble E. P., 1926, ApJ, 64, 321
Kannan R., Stinson G. S., Macciò A. V., Brook C., Weinmann S. M., Wadsley J., Couchman H. M. P., 2014, MNRAS, 437, 3529
Karim A. et al., 2011, ApJ, 730, 61
Kelson D. D., 2014, preprint (arXiv:1406.5191)
Kennicutt R. C., Evans N. J., 2012, ARA&A, 50, 531
Kennicutt R. C., Jr, 1989, ApJ, 344, 685
Kennicutt R. C., Jr, 1998, ApJ, 498, 541
Kereš D., Vogelsberger M., Sijacki D., Springel V., Hernquist L., 2012, MNRAS, 425, 2027
Klypin A. A., Trujillo-Gomez S., Primack J., 2011, ApJ, 740, 102
Knapen J. H., James P. A., 2009, ApJ, 698, 1437
Kravtsov A., Vikhlinin A., Meshscheryakov A., 2014, preprint (arXiv:1401.7329)
Labbé I. et al., 2010, ApJ, 716, L103
Lilly S. J., Le Fevre O., Hammer F., Crampton D., 1996, ApJ, 460, L1
Lilly S. J., Carollo C. M., Pipino A., Renzini A., Peng Y., 2013, ApJ, 772, 119
Madau P., Pozzetti L., Dickinson M., 1998, ApJ, 498, 106
Mannucci F., Cresci G., Maiolino R., Marconi A., Gnerucci A., 2010, MNRAS, 408, 2115
Marinacci F., Pakmor R., Springel V., 2014, MNRAS, 437, 1750
Michałowski M. J., Dunlop J. S., Cirasuolo M., Hjorth J., Hayward C. C., Watson D., 2012, A&A, 541, A85
Michałowski M. J., Hayward C. C., Dunlop J. S., Bruce V. A., Cirasuolo M., Cullen F., Hernquist L., 2014, A&A, 571, A75
Mihos J. C., Hernquist L., 1996, ApJ, 464, 641
Mitchell P. D., Lacey C. G., Cole S., Baugh C. M., 2014, MNRAS, 444, 2637
Mitra S., Davé R., Finlator K., 2014, preprint (arXiv:1411.1157)
Moster B. P., Naab T., White S. D. M., 2013, MNRAS, 428, 3121
Nelson D., Vogelsberger M., Genel S., Sijacki D., Kereš D., Springel V., Hernquist L., 2013, MNRAS, 429, 3353
Noeske K. G. et al., 2007, ApJ, 660, L47
Patton D. R., Torrey P., Ellison S. L., Mendel J. T., Scudder J. M., 2013, MNRAS, 433, L59
Pillepich A. et al., 2014, MNRAS, 444, 237
Porter L. A., Somerville R. S., Primack J. R., Johansson P. H., 2014, MNRAS, 444, 942
Puech M., Hammer F., Rodrigues M., Fouquet S., Flores H., Disseau K., 2014, MNRAS, 443, L49
Rees M. J., Ostriker J. P., 1977, MNRAS, 179, 541
Rodighiero G. et al., 2011, ApJ, 739, L40
Sakamoto K. et al., 2008, ApJ, 684, 957
Salim S. et al., 2007, ApJS, 173, 267
Sanders D. B., Soifer B. T., Elias J. H., Madore B. F., Matthews K., Neugebauer G., Scoville N. Z., 1988, ApJ, 325, 74
Sargent M. T., Béthermin M., Daddi E., Elbaz D., 2012, ApJ, 747, L31
Schawinski K. et al., 2014, MNRAS, 440, 889
Schaye J. et al., 2010, MNRAS, 402, 1536
Schaye J. et al., 2015, MNRAS, 446, 521
Schmidt M., 1959, ApJ, 129, 243
Scudder J. M., Ellison S. L., Torrey P., Patton D. R., Mendel J. T., 2012, MNRAS, 426, 549
Sijacki D., Springel V., Di Matteo T., Hernquist L., 2007, MNRAS, 380, 877
Sijacki D., Vogelsberger M., Kereš D., Springel V., Hernquist L., 2012, MNRAS, 424, 2999
Silk J., 1977, ApJ, 211, 638
Simha V., Weinberg D. H., Conroy C., Dave R., Fardal M., Katz N., Oppenheimer B. D., 2014, preprint (arXiv:1404.0402)
Speagle J. S., Steinhardt C. L., Capak P. L., Silverman J. D., 2014, ApJS, 214, 15
Springel V., 2010, MNRAS, 401, 791
Springel V., Hernquist L., 2003, MNRAS, 339, 289
Springel V., Di Matteo T., Hernquist L., 2005a, MNRAS, 361, 776
Springel V. et al., 2005b, Nature, 435, 629
Strateva I. et al., 2001, AJ, 122, 1861
Tasca L. A. M. et al., 2014, preprint (arXiv:1411.5687)
Toft S. et al., 2014, ApJ, 782, 68
Torrey P., Cox T. J., Kewley L., Hernquist L., 2012, ApJ, 746, 108
Torrey P., Vogelsberger M., Genel S., Sijacki D., Springel V., Hernquist L., 2014a, MNRAS, 438, 1985
Torrey P. et al., 2014b, preprint (arXiv:1411.3717)
Tremonti C. A. et al., 2004, ApJ, 613, 898
Tully R. B., Fisher J. R., 1977, A&A, 54, 661
Vogelsberger M., Sijacki D., Kereš D., Springel V., Hernquist L., 2012, MNRAS, 425, 3024
Vogelsberger M., Genel S., Sijacki D., Torrey P., Springel V., Hernquist L., 2013, MNRAS, 436, 3031
Vogelsberger M. et al., 2014a, MNRAS, 444, 1518
Vogelsberger M. et al., 2014b, Nature, 509, 177
Whitaker K. E., van Dokkum P. G., Brammer G., Franx M., 2012, ApJ, 754, L29
White S. D. M., Rees M. J., 1978, MNRAS, 183, 341
Wuyts S. et al., 2011, ApJ, 742, 96
Zel'dovich Y. B., 1970, A&A, 5, 84

This paper has been typeset from a TEX/LATEX file prepared by the author.